

# Full Wave Monostatic Radar Cross Section Computation for Challenging RF Problems

Mark Whale<sup>1</sup>, Edoardo Baldazzi<sup>1</sup>, Cecilia Cappelin<sup>1</sup>, Martin Haulund Gaede<sup>1</sup>,  
and Oscar Borries<sup>1</sup>.

(1) TICRA, Landemærket 29, 1119 Copenhagen, Denmark.

**Abstract**—Radar Cross Section (RCS) computation plays a critical role in the design and analysis of scattering objects in both civilian and military applications. Reliable and efficient simulation tools enable RCS minimization during the design phase, reducing reliance on measurements to the final stages of development. Two main classes of techniques are typically used for RCS prediction: high-frequency asymptotic methods and full-wave numerical methods. Unlike high-frequency approximations, full-wave methods such as the Method of Moments (MoM) provide highly accurate results by rigorously solving Maxwell's equations removing any approximation. However, their application to electrically large problems is limited by high computational and memory cost.

In this paper we present results from an efficient and accurate full-wave solver when computing the monostatic RCS of electrically large structures. The solver employs higher-order basis functions to reduce the number of unknowns and the Multilevel Fast Multipole Method (MLFMM) to significantly lower memory usage and computational time. Additionally a new so-called Fast Direct Solver (FDS) is utilised for a smaller selection of these RCS calculations. After a brief description of the implementation, several application cases are presented and validated against measurements and benchmarks, demonstrating the capability to handle complex scenarios with short simulation times and cost-effective hardware.

**Index Terms**—radar cross section, full wave solver, Method of Moments, rcs, MLFMM, Fast Direct Solver.

## I. INTRODUCTION

The monostatic RCS computation is an important part of the engineering process in many applications. The growing field of automotive radars can benefit from RCS predictions or measurements to enrich the database for processing units. Alternatively, RCS can be used as a design constraint for antenna systems by using periodic structures like reflectarrays and trasmittarrays. RCS values are used in radar application to predict or estimate how targets are detectable, typically employed for but not limited to aircraft. For electrically large structures, asymptotic methods have been commonly used [1]-[3]. However, such methods, when complex shapes are involved, fail to describe properly the scattering phenomena, thus a more rigorous solution using full-wave methods such as MoM is desirable. To overcome the typical limitations of high computational and memory costs for such a method, a more efficient solver specifically for monostatic RCS computation has been developed.

In this contribution, the ESTEAM software [4], belonging to the TICRA Tools suite, is used to evaluate the monostatic RCS of some geometries considered from typical operative scenarios. This software utilises both the direct solver implementations i.e., Method of Moments (MoM), and a Multilevel Fast Multipole Method (MLFMM), which employs higher-order basis functions to reduce the number of unknowns to significantly lower memory usage and computational time. Additionally, a recently developed Fast Direct Solver (FDS) that improves upon computational efficiency of both MoM and MLFMM is presented for two electrically large structures in this work.

## II. MONOSTATIC RADAR CROSS SECTION

RCS calculation implemented in ESTEAM is based on the following definition for any arbitrary direction  $(\theta_r, \phi_r)$ :

$$\sigma(\theta_r, \phi_r) = \lim_{r \rightarrow \infty} 4\pi r^2 \frac{|\mathbf{E}^S(\theta_r, \phi_r)|^2}{|\mathbf{E}^I(\theta_i, \phi_i)|^2} \quad (1)$$

where  $\mathbf{E}^S$  is the scattered field and  $\mathbf{E}^I$  is the incident one, being a plane wave from direction  $(\theta_i, \phi_i)$ . Taking into account polarisation of the incident and scattered fields, (2) is updated accordingly to

$$\sigma(\theta_r, \phi_r)_{\psi v} = \lim_{r \rightarrow \infty} 4\pi r^2 \frac{|\mathbf{E}^S(\theta_r, \phi_r) \cdot \hat{\psi}|^2}{|\mathbf{E}_v^I(\theta_i, \phi_i)|^2} \quad (2)$$

where  $\mathbf{E}_v^I(\theta_i, \phi_i)$  is incident electric field (plane wave) polarised in the  $v$  direction. Commonly the polarisation vectors are chosen as  $\hat{\psi}, \hat{v}$  the spherical unit vectors such that  $\hat{\psi}, \hat{v} = \hat{\theta}, \hat{\phi}$ . Considering the monostatic case, where  $(\theta_i = \theta_r, \phi_i = \phi_r)$ , implies the incident plane wave illuminates the object of interest and the resultant scattered field in the same direction is sampled. This introduces significant computational load, requiring a computation for each desired incident direction.

### A. Full-wave methods for RCS calculation

Full-wave methods based on integral equation formulations are desirable in terms of their higher accuracy, in particular when considering structures that contribute to multiple scatterings and creeping waves, such as would be observed with duct-like structures common to aircraft fuselages. The full-wave problem is solved using integral equations for time harmonic fields. For perfectly conducting scatterers (PEC) the mixed potential Electrical Field Integral Equations (EFIE) are

used, while for closed sections the Combined Field Integral Equations (CFIE) are employed. For scatterer objects with dielectric properties, surface integral equations are employed based on the PMCHWT formulation which ensures proper field continuity across dielectric interfaces [6], [7]. For monostatic RCS with  $P$  incidence angles, the system contains  $P/2$  right-hand sides (RHSs) and can be written as:

$$\overline{\overline{Z}}\overline{\overline{I}} = \overline{\overline{V}} \quad (3)$$

where  $\overline{\overline{Z}}$  has size  $N \times N$  and  $\overline{\overline{I}}, \overline{\overline{V}}$  have size  $N \times P$ , and  $N$  is the number of unknowns. Using a direct solver approach i.e., MoM, implies a computational complexity  $\mathcal{O}(f^6)$ , where  $f$  is the frequency, which for electrically large problems becomes challenging. Avoidance of this asymptotic scaling is realised with an acceleration method in MLFMM, wherein the impedance matrix (3) is solved iteratively [5], consequently reducing computational complexity to  $\mathcal{O}(C(f, P)f^2 \log f)$ , where  $C(f, P)$  is the number of iterations for convergence. The MLFMM algorithm developed in ESTEAM includes a discretisation based on higher-order basis functions and curved quadrilaterals, thereby maintaining low memory requirements. A further reduction in complexity is realised through the following compression of the RHS matrix:

$$\overline{\overline{V}} \approx \overline{\overline{C}}\overline{\overline{D}} \quad (4)$$

where  $\overline{\overline{C}}$  has size  $N \times P_c$  and  $\overline{\overline{D}}$  has size  $P_c \times P$ , with  $P_c$  being the number of RHS after compression. As such, the iterative solver applied to  $P_c$  RHSs will reduce overall complexity.

The Fast Direct Solver (FDS) is an efficient approach for solving MoM equations through approximation of the system matrix which allows for solving multiple RHSs [8]. With higher-order discretizations of the CFIE and adopting higher-order polynomials with MoM the number of unknowns is significantly reduced, thereby reducing the calculation time for RCS calculations. In this work we compare the results for the FDS against the MLFMM for two target bodies, detailed in Section III-G.

### III. APPLICATION EXAMPLES

In this section the results of monostatic RCS calculations on multiple targets; both PEC and full dielectric, and a combination of the two, are presented. For clarity to the reader, when referring to the numbered sections of this paper we use 'Section' as an identifier, while when referring to those benchmark test cases which use a similar official numbering scheme we use 'Case' and 'Problem Set' as the identifiers where applicable.

These calculations range from so-called benchmarks [11] to more real-world examples applications [14]. In Sections III-A, III-B, and III-C benchmark test cases from the Austin RCS series are calculated. In Section III-D so-called benchmark Ogive structures are calculated with comparisons drawn against the results from literature. In case III-E a full PEC waveguide horn and full dielectric truncated prism are calculated and compared against the reference sources [15],[16]. Case III-F presents a

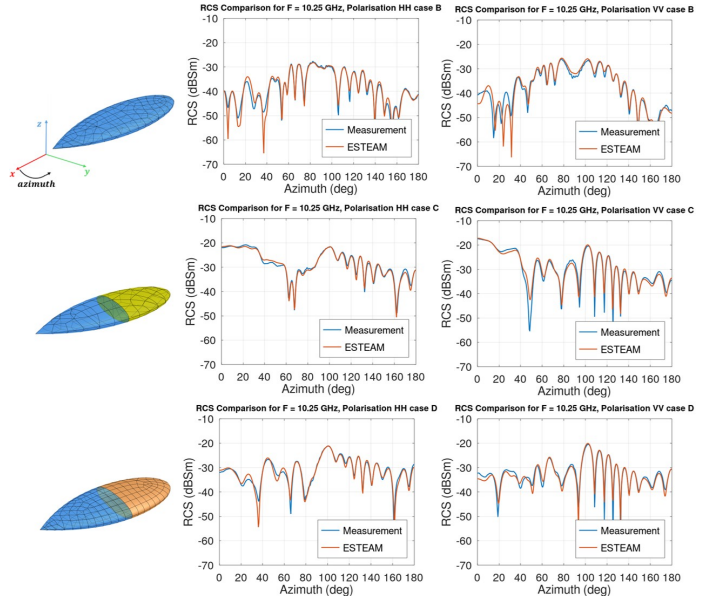


Figure 1: RCS results at 10.25 GHz for NASA Almonds from Austin's problem set III. On the left side ESTEAM mesh plot is shown for each case. Starting from the top, a fully dielectric almond is presented denoted with colour blue is Case III-B. The half dielectric and half closed PEC region comprises Case III-C, where PEC region is shown in yellow. Finally, Case III-D involves a dielectric almond with PEC coated tail (colour orange)

newly proposed benchmark model from [14] of a combined dielectric radome that surrounds a PEC structure, and finally in case III-G a consumer-level drone device is simulated. The RCS calculations presented are from combinations of MoM, MLFMM, and FDS.

#### A. Austin RCS Benchmarks: Problem Set III

In this section, RCS calculations of the so-called NASA almonds benchmarks from [11] are presented. Three cases are selected: case III-B is fully dielectric, case III-C is a half dielectric and PEC, and case III-D a dielectric almond with a PEC coated tail. Figure 1 shows RCS simulations, at 10.25 GHz, of each case with dielectric region having  $\epsilon' = 2.88$  and  $\epsilon'' = 7.85 \times 10^{-2}$  and an overall length of 252.37 mm. Simulation results were calculated using the direct MoM solver and results are in excellent agreement with measurements provided in [11].

#### B. Austin RCS Benchmarks: Problem Set IIIS

In this section, the following shapes are modelled: a box with a curved duct, a box with a cylindrical cavity and a box with the same cylindrical cavity featuring a detailed fan inside. Each shape is modelled as a closed PEC region in the 3D mesh, having a length of 40 cm to match the measured prototype. The first two shapes are simulated using the direct MoM solver and the RCS results demonstrate excellent agreement to reference measurements (see Figure 2). The MLFMM

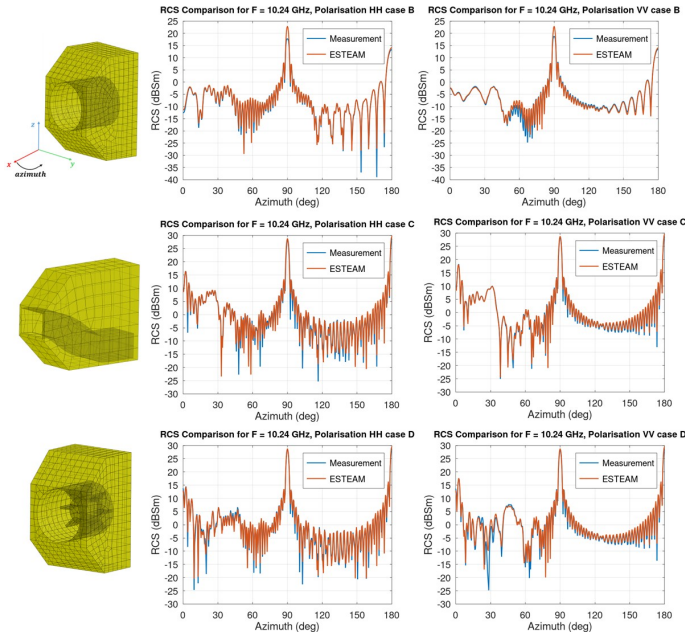


Figure 2: RCS values at 10.24 GHz for Austin's problem set IIS models. On the left side ESTEAM mesh plot is shown for each case.

solver is utilised for the last shape and it is notable that the resultant calculation was achieved with a compression of the number of directions from 361 to 68. The resultant high agreement with measurements together with the significant reduction in computational complexity demonstrates clearly the effectiveness of the MLFMM solver implementation.

### C. Austin RCS Benchmarks: Problem Set IV

An additional RCS benchmark provided in [11]-[12] is the reProducible pRIntable electroMagnEtic (PRIME) airplane model, being a simplified airplane with either closed or open ducts. Benchmarks for the scaled versions of the plane model with an overall length (nose-to-tail) equal to 254 mm are analysed here. Strong agreement is obtained with the measurements reported (see Figure 3) for both geometries. The results presented have been computed with a workstation featuring an AMD Ryzen 9 5950X CPU, with 16 physical cores and 32 logical cores.

### D. Radar Targets Benchmark (Ogive)

In [13] radar targets resembling actual shapes in common operational scenarios have been analysed and measured to benchmark RCS simulations. The single and double ogives, cone-sphere, and cone-sphere with gap targets are simulated and compared against measurements in Figures 4 and 5. Again a high level agreement between predicted values and the results from literature is observed in all cases. Run times for these shapes were significantly reduced due to their being described readily with Body-of-Revolution (BoR) MoM in ESTEAM, which ensures a significantly simpler mesh description

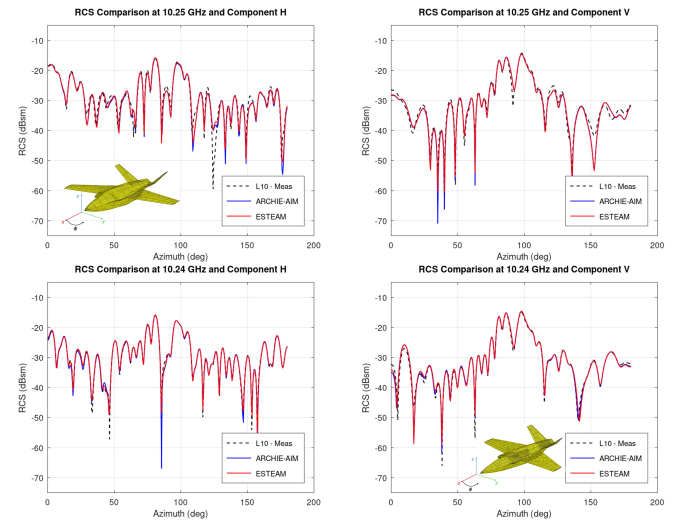


Figure 3: Closed-Ducts (Top) and Open-Ducts (Bottom) RCS values obtained from ESTEAM simulation at 10.25 GHz and 10.24 GHz for both vertically and horizontally (denoted as component V and H) plane waves response. Results (solid red line) are compared to Austin's ARCHIE-AIM software (solid blue line) and published measurements (dashed black line).

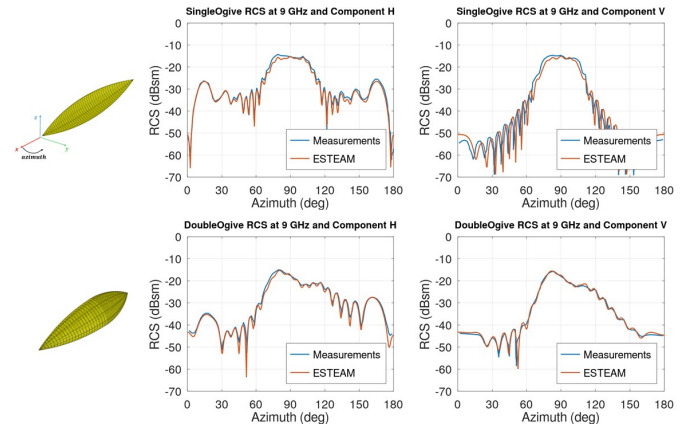


Figure 4: Single (Top) and Double (Bottom) ogive RCS values obtained from ESTEAM simulation at 9 GHz for both vertically and horizontally (denoted as component V and H) plane waves response. Results (solid red line) are compared with available measurements (solid blue line) in [13].

with no reduction in accuracy. Simulations were run on a mid-to-high end laptop with Intel core i9-12900HK CPU and 64 GB of physical memory.

### E. Waveguide Horn and Truncated Prism

As part of the European Defence Agency (EDA) workshop entitled "Radar Signatures & EM Benchmarks", new and updated test cases for RCS benchmarks are routinely proposed [15], [16]. In [16], a standard commercially available rectangular horn antenna was both modelled and measured. The CAD model for this horn, provided by the responsible

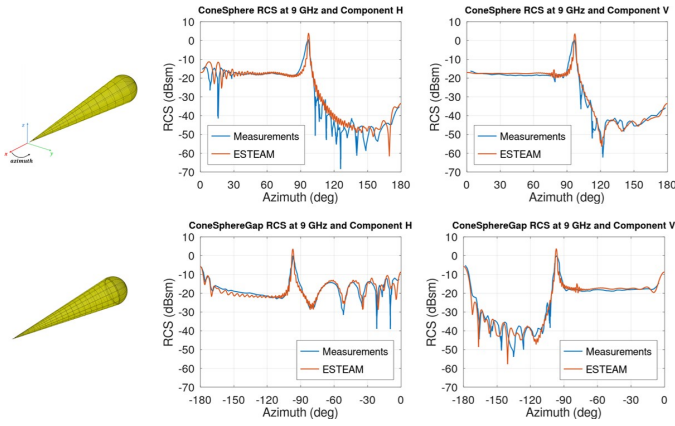


Figure 5: Cone-sphere (Top) and Cone-sphere with gap (Bottom) RCS values obtained from ESTEAM simulation at 9 GHz for both vertically and horizontally (denoted as component V and H) plane waves response. Results (solid red line) are compared with available measurements (solid blue line) in [13].

parties at the Fraunhofer Institute, was analysed at 9 GHz with the direct MoM solver in ESTEAM and compared against the equivalent simulation results in Figure 6.

Similarly, a truncated dielectric prism was developed for [15]. The details of this model were obtained and compared against the original measurement data, provided by responsible parties at Instituto Nacional de Técnica Aeroespacial (INTA) in Spain. It is observed that while there are some notable discrepancies between measurement and simulations in the results for the prism, these are equivalent to the same discrepancies reported by other simulation results submitted to [14] and [16] and are ascribed to deviations in measurement setup compared with the idealised simulations.

#### F. Ogive Radome

From [16] and highlighted in [14], a novel test case called the Ogive Radome was introduced. This object represents a nose-cone shape of an aircraft or similar aerodynamic device that encloses an array-based radar platform, as illustrated in Figure 7. The cone shape is a dielectric shell mounted over an obliquely truncated PEC cylinder. The tilted top surface is intended to represent the surface of a planar phased array typical in defence radar applications. The dimensions of the overall shape coupled with the resonant nature of the structure make this a computationally challenging problem at the frequencies of interest in [14] i.e., 5, GHz, 10 GHz and 15 GHz. In Figure 7 results from MLFMM simulations for 10 GHz are compared against equivalent simulations presented in [14], provided by the responsible parties at the Swedish Defense Research Agency (FOI). These RCS calculations were performed on a system with a Dual Xeon Gold 5218 2.3 GHz processor with 32 CPU threads. With this system, the runtimes for a converged model of the Ogive providing all polarisation combinations for a half-circle in  $\theta$  with 1 degree steps were

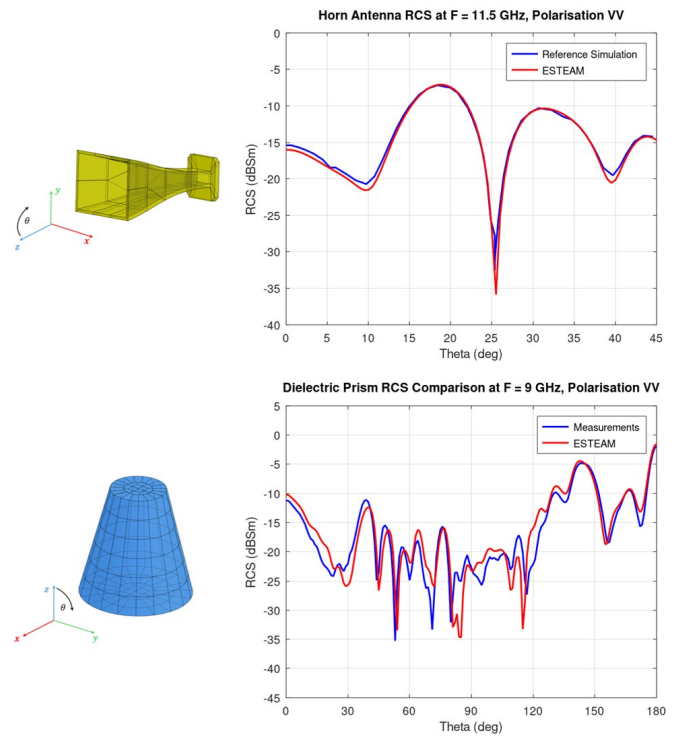


Figure 6: Horn antenna (Top) and dielectric prism (bottom) RCS values at 11.5 GHz and 9 GHz, respectively.

12 minutes for 5GHz, 3 hours 5 minutes for 10 GHz, and 11 hours 22 minutes for 15 GHz.

#### G. Drone

With inspiration from [17] a CAD model of a typical consumer-grade drone was implemented and three variations were analysed: a full PEC, a full dielectric, and a dielectric body with PEC payload. The dielectric material used a permittivity of 2.95 with loss tangent of 0.0001 to best represent reinforced carbon fibre plastics. These three models and their corresponding results at 26 and 40 GHz are provided in Figure 8. The impact of the different compositions the drone to the monostatic RCS is clearly demonstrated with this simulation. These simulations were performed with either direct MoM, as for the full PEC model, or MLFMM for fully dielectric and dielectric plus PEC payload, and the times are reported accordingly in Tables I and II. Moreover, to appreciate the benefit from the compression of RCS directions implemented in the MLFMM, case C) has been simulated with full 722 directions. This computation required approximately 10 hours while with no compression, while with compression completed in approximately 2.5 hours, thus a time saving of 75% with no loss in accuracy. As a demonstration of a newly developed FDS algorithm the two MLFMM cases were also modelled with this new solver. The results of this simulation are shown in Figure 9 and show strong agreement with the MLFMM equivalent. Furthermore, computational times are significantly reduced in comparison to MLFMM. For example, for the full dielectric drone at 26 GHz the computation time was reduced

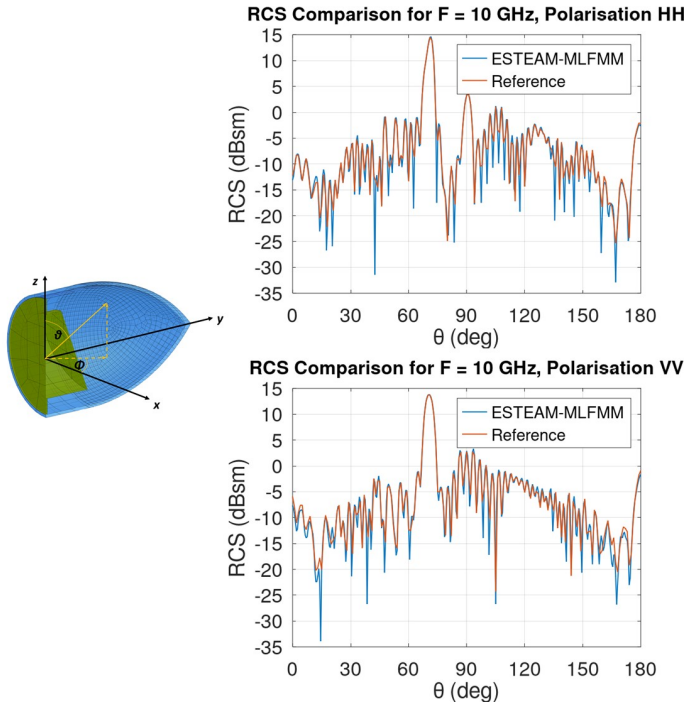


Figure 7: Ogive Radome structure (left) with a cutout in  $yz$  plane showing the internal structure of the truncated PEC cone (yellow) encased in a dielectric shell of ogive shape (blue). The resultant RCS calculations (right) are compared against the reference simulation from [14] at 10GHz

from 227 minutes with MLFMM to 65 minutes with FDS for the same computational machine, representing a significant improvement to the computational efficiency.

#### IV. CONCLUSIONS

An introduction to the approach to RCS simulations in the TICRA software ESTEAM was presented, with details and references provided for the MoM, MLFMM, and FDS algorithms. Multiple RCS simulations on a variety of shapes and target structures were performed and comparisons made with results of measurements and reference simulations from the source literatures, with excellent agreement throughout. The computational efficiencies of each case is reported for reference to the reader with explicit details of computational machines, memory, times and other pertinent information. Results from the new FDS algorithm indicate a significant improvement in computational efficiency with no loss in accuracy in comparison to the equivalent MLFMM results. It is expected to continue with benchmarking activities using the FDS implementation and expand these activities to future publications.

#### ACKNOWLEDGEMENT

Thanks and appreciation is extended to Johannes Boeckler at the Fraunhofer Institute for providing the CAD model of the Horn Antenna in Section III-E, David Poyatos Martines at INTA for providing measurement data of the Dielectric Prism,

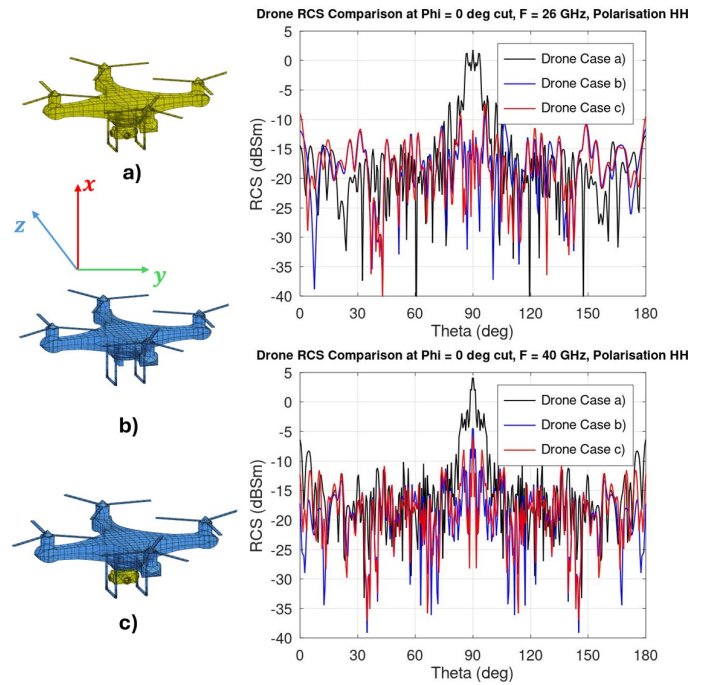


Figure 8: RCS values of a drone assumed with a payload. Three cases are presented: full PEC model (a), the drone without the payload and considered fully dielectric (b) and the dielectric drone with its PEC payload. Results are shown at 26 GHz and 40 GHz on the phi 0 degree plane.

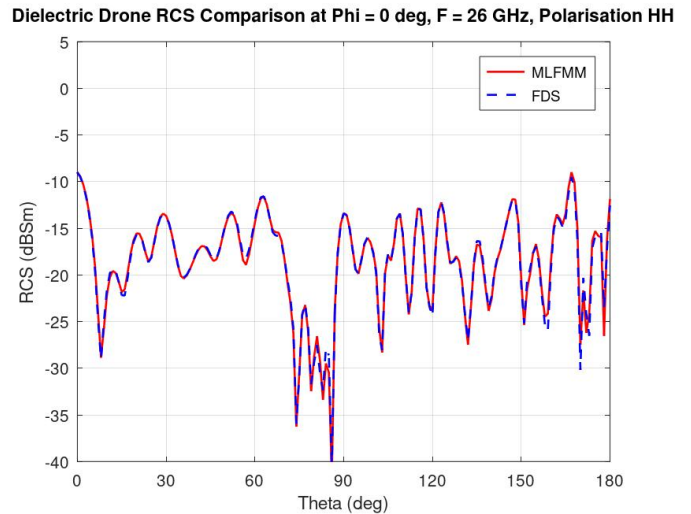


Figure 9: RCS data for the fully dielectric drone comparing the results from MLFMM and FDS algorithms.

also in Section III-E, and to Magnus Gustavsson at FOI for providing the CAD model and comparative simulation data for the Ogive Radome in Section III-F.

Table I: Direct MoM simulation details and computational resources required to evaluate RCS. A selection of the presented geometries are shown in the table reporting the size of the problem. N is the total number of MoM unknowns.

Geometry	Freq. (GHz)	Size in $\lambda_0$	N	RCS Directions	Time (min)	Memory (GB)	Platform (Tab. III)
Austin Case IIB	7 10.25	5.9 8.6	15566 32358	361	1 3	2.4 7.8	(1)
Austin Case IIS-C	7 10.24	9.3 13.6	15050 27073	361	1 3	1.7 5.5	(1)
Austin Case IV-B	7 10.24	5.8 8.5	5300 19294	361	1 3	3.5 2.8	(3)
Double Ogive	1.57 9	1 5.7	1960 5570	361	0.1 0.1	0.03 0.24	(1)
Cone-Sphere with Gap	0.869 9	1.9 20.6	1240 13806	361	0.08 0.5	0.001 1.4	(1)
Dielectric Prism	9	6	22266	361	1.4	3.7	(1)
Drone (a)	26 40	29 44.6	22501 41797	722	1 4.5	3.8 13	(3)

Table II: MLFMM simulation details and computational resources required to evaluate RCS. N is the total number of unknowns while the compressed directions reports the final number of directions simulated by MLFMM.

Geometry	Freq. (GHz)	Size in $\lambda_0$	N	RCS Directions	Compressed Directions	Time (min)	Memory (GB)	Platform (Tab. III)
Dielectric Ogive	10 15	16.6 25	173301 396798	181 181	63 88	185 682	9.9 12	(2) (2)
Austin Case IIS-D	10.24	21.8	77501	361	68	50	5	(3)
Drone (b)	26 40	29 44.6	95160 213600	722 362	169 130	154 477	3.5 11	(3)
Drone (c)	26 40	29 44.6	96667 216244	722 362	169 130	227 732	3.9 12	(3)

Table III: Hardware platforms used to compute RCS values.

Platform	Specifications
(1)	Intel Core i9-12900HK 14-Cores - 64 GB
(2)	Intel Core i9-14900KF 24-Cores - 192 GB
(3)	AMD Ryzen 9 5950X 16-Cores - 128 GB RAM

## REFERENCES

- [1] Y. An, D. Wang, and R. Chen, "Improved multilevel physical optics algorithm for fast computation of monostatic radar cross section," *IET Microwaves, Antennas & Propagation*, vol. 8, pp. 93–98, Jan. 2014.
- [2] M. S. Pavlovic, M. S. Tasic, B. L. Mrdakovic, and B. M. Kolundžija, "WIPL-D: Monostatic RCS Analysis of Fighter Aircrafts," *2016 10th European Conference on Antennas and Propagation (EuCAP)*.
- [3] K. Divyabramham and R. Vulapalli, RCS Predictions for Electrically Large Complex Structures. [Online]. Available: <https://goo.gl/81QH5X>
- [4] ESTEAM, <https://www.ticra.com/software/esteem/>.
- [5] Y. Saad and M. H. Schultz, "GMRES: A Generalized Minimal Residual Algorithm for Solving Nonsymmetric Linear Systems," *SIAM J. Sci. Comput.*, vol. 7, no. 3, pp. 856–869, Jun. 1986
- [6] Mautz, J. R. & Harrington, R. F., "Electromagnetic Scattering From a Homogeneous Material Body of Revolution", 1979, *Archiv Elektronik und Uebertragungstechnik*, 33, 71.
- [7] Te-Kao Wu, Leonard L. Tsai, "Scattering from arbitrarily-shaped lossy dielectric bodies of revolution", *Radio Science*, Vol. 12, Issue 5, pp. 709–718, Oct. 1977.
- [8] M. H. Gæde, M. S. Andersen, A. Limkilde, O. Borries, J. S. Hesthaven, "A Fast Direct Solver for Higher Order Discretizations of Integral Equations", *IEEE Int. Symp. on Antennas and Propagation and USNC-URSI Radio Science Meeting*, Florence, Italy, 2024, doi: 10.1109/AP-S/INC-USNC-URSI52054.2024.10686430
- [9] O. Borries, E. Jorgensen and P. Meincke, "Monostatic RCS of electrically large structures using higher-order MLFMM," *2017 11th European Conference on Antennas and Propagation (EuCAP)*, Paris, France, 2017, pp. 872–876, doi:10.23919/EuCAP.2017.7928658.
- [10] A. Limkilde, O. Borries, P. Meincke and E. Jørgensen, "Full-Wave Monostatic Radar Cross Section using the Multilevel Fast Multipole Method," *2023 17th European Conference on Antennas and Propagation (EuCAP)*, Florence, Italy, 2023, pp. 1–5, doi: 10.23919/EuCAP57121.2023.10133305.
- [11] "Austin Benchmark Suites for Computational Electromagnetics," 2018. [Online]. Available - <https://github.com/UTAustinCEMGroup/AustinCEMBenchmarks/tree/master/Austin-RCS-benchmarks/Problem%20IV-PRIME%20Aircrafts>.
- [12] A. Maicke et al., "A Benchmark Airplane Model with Ducts," *2022 IEEE International Symposium on Antennas and Propagation and USNC-URSI Radio Science Meeting (AP-S/URSI)*, Denver, CO, USA, 2022.
- [13] A. C. Woo, H. T.G. Wang, M. J. Schuh, and M. L. Sanders. "Benchmark Plate Radar Targets for the Validation of Computational Electromagnetics Programs," *IEEE Antennas and Propagation Magazine*, vol. 35, no. 1, February 1993.
- [14] F. Weinmann et al., "The European Defence Agency Workshop "Radar Signatures & EM Benchmarks": A scientific forum for comparison and evaluation of electromagnetic simulations," in *IEEE Antennas and Propagation Magazine*, vol. 67, no. 2, pp. 43–50, April 2025, doi: 10.1109/MAP.2025.3537408.
- [15] "EDA-workshop 'Radar signatures & EM benchmark'," EDA Facilities, Brussels, Belgium, Nov. 2019 [Online]. Available: <https://www.fhr.fraunhofer.de/en/events/2019/eda-workshop-radar-signatures-and-em-benchmarks.html>.
- [16] "EDA-workshop 'Radar signatures & EM benchmark'," Fraunhofer FHR, Wachtberg, Germany, Jun. 2023 [Online]. Available: <https://www.fhr.fraunhofer.de/de/veranstaltungen/2023/eda-workshop-2023-radar-signatures-and-em-benchmarks.html>.
- [17] V. Semkin et. al., "Analyzing Radar Cross Section Signatures of Diverse Drone Models at mmWave Frequencies," *IEEE Access*, vol. 8, pp. 48958 – 48969, 11 Mar. 2020, doi: 10.1109/ACCESS.2020.2979339